

One EURO for Uranus: the Elliptical Uranian Relativity Orbiter mission

Lorenzo Iorio¹

Ministero dell' Istruzione e del Merito
Viale Unità di Italia 68, I-70125, Bari (BA), Italy

Athul Pradeepkumar Girija

Purdue University, West Lafayette, IN 47907, USA

Daniele Durante

Department of Mechanical and Aerospace Engineering, Sapienza University of Rome, Rome,
Italy

Received _____; accepted _____

arXiv:2303.00812v3 [gr-qc] 11 May 2023

¹Corresponding author. Email: lorenzo.iorio@libero.it

Abstract

Recent years have seen increasing interest in sending a mission to Uranus, visited so far only by Voyager 2 in 1986. EURO (Elliptical Uranian Relativity Orbiter) is a preliminary mission concept investigating the possibility of dynamically measuring the planet's angular momentum by means of the Lense-Thirring effect affecting a putative Uranian orbiter. It is possible, at least in principle, to separate the relativistic precessions of the orbital inclination to the Celestial Equator and of the longitude of the ascending node of the spacecraft from its classical rates of the pericentre induced by the multipoles of the planet's gravity field by adopting an appropriate orbital configuration. For a wide and elliptical $2\,000 \times 100\,000$ km orbit, the gravitomagnetic signatures amount to tens of milliarcseconds per year, while, for a suitable choice of the initial conditions, the peak-to-peak amplitude of the range-rate shift can reach the level of $\approx 1.5 \times 10^{-3}$ millimetre per second in a single pericentre passage of a few hours. By lowering the apocentre height to 10 000 km, the Lense-Thirring precessions are enhanced to the level of hundreds of milliarcseconds per year. The uncertainties in the orientation of the planetary spin axis and in the inclination are major sources of systematic bias; it turns out that they should be determined with accuracies as good as $\approx 0.1 - 1$ and $\approx 1 - 10$ milliarcseconds, respectively.

Subject headings: Gravitation – planets and satellites: individual: Uranus – space vehicles

1. Introduction

So far, Uranus (Bergstrahl, Miner & Matthews 1991; Hubbard 1997), the seventh planet of our solar system discovered in the eighteenth century (Herschel 1781), has been visited by an automated spacecraft only once when, in January 1986, the NASA probe Voyager 2 flew closely past it (Stone & Miner 1986; Stone 1987).

Recent years have seen a renewed interest for the exploration of Uranus and, possibly, Neptune¹ (Cruikshank 1995), discovered in the mid of the nineteenth century (Le Verrier 1846; Galle 1846), boosting a number of investigations of possible spacecraft-based missions, submitted mostly to NASA and ESA, targeted to at least one or both the two icy giants (National Research Council 2011; Mousis et al. 2018; National Research Council 2018; Fletcher et al. 2020; Gibney 2020; Tacconi et al. 2021; National Research Council 2022; Witze 2022; Hofstadter et al. 2019; Guillot 2021). Their main targets are a better knowledge of the fundamental physical parameters of the most distant Sun’s planets, such as their gravitational and magnetic fields, rotation rates, and deep atmospheric composition and temperature (Helled, Nettelmann & Guillot 2020), and of their natural satellites, many of them may be icy ocean worlds that could possibly harbor life (Mann 2017). At present, none of such proposals was approved by any space agency.

Here, we make a cursory overview of some of the past proposals. Among them, there was the Uranus Pathfinder concept for an Uranian orbiter (Arridge et al. 2012), submitted in 2011 to ESA as a M-class mission. ODINUS (Origins, Dynamics, and Interiors of the Neptunian and Uranian Systems) was proposed to the ESA’s Cosmic Vision programme in 2013 as a L-class mission aimed at sending two twin orbiters around Uranus and Neptune, respectively (Turrini et al. 2014). The science case for an orbital mission to Uranus only, rooted in the ODINUS concept, was explored in a separated study (Arridge et al. 2014). MUSE (Mission to Uranus for Science and Exploration) was another proposal to ESA for a L-class mission to Uranus (Bocanegra-Bahamón et al. 2015). A further mission concept implying an Uranian orbiter, proposed to NASA in 2017, was OCEANUS (Origins and Composition of the Exoplanet Analog Uranus System) (Mansell et al. 2017). A multi-probe mission to Uranus, including a SNAP (Small Next-Generation Atmospheric Probe), was studied by Sayanagi et al. (2020). QUEST (Quest to Uranus to Explore Solar System Theories) is a lower cost option for a flagship mission aimed to insert an orbiter around Uranus arisen during the 30th Annual NASA/JPL Planetary Science Summer Seminar (Jarmak et al. 2020).

At the time of writing, it seems that the latest proposal for a mission targeted at Uranus, submitted to NASA, is UOP (Uranus Orbiter and Probe) (Simon, Nimmo & Anderson 2021; Mandt 2023); it is giving rise to a number of related studies (Cohen et al. 2022; Girija 2023). Preliminary hints of a possible flyby of Uranus with a future Chinese interplanetary exploration

¹In general, missions to Uranus are favored due to logistical and cost reasons.

mission beyond Jupiter can be found in² Xu, Zou & Jia (2018).

Among the physical parameters of interest of Uranus (and Neptune), whose determination/constraint is the main goal of the aforementioned proposed missions, there are the (normalized) moment of inertia (MoI) \mathcal{J} and the rotation period P (Helled & Fortney 2020; Helled, Nettelmann & Guillot 2020; Neuenschwander & Helled 2022). In general, they depend on the distribution of matter in the interior of a planet, concurring to form its spin angular momentum

$$S = \mathcal{J} M R^2 \omega, \quad (1)$$

where M is the planet’s mass, R is its equatorial radius, and

$$\omega \doteq \frac{2\pi}{P} \quad (2)$$

is its rotational angular speed. Neuenschwander & Helled (2022) pointed out that a determination of the Uranian MoI $\mathcal{J}_{\hat{\delta}}$ at a $\approx 1 - 0.1$ per cent level could constrain the planetary rotation period and the depth of the winds, respectively. Neuenschwander & Helled (2022) acknowledged that it is not an easy task which could be implemented only with a future dedicated space mission.

General relativity³ (Misner, Thorne & Wheeler 2017) offers, in principle, a way to measure the spin angular momentum S of a rotating body in a dynamical, model-independent way. Indeed, in its weak-field and slow-motion approximation, its linearized equations formally resemble those of the Maxwellian electromagnetism giving rise to the so-called “gravitoelectromagnetic” paradigm. For such a concept within the framework of the Einsteinian theory of gravitation, see, e.g., Cattaneo (1958); Thorne, MacDonald & Price (1986); Thorne (1986, 1988); Harris (1991); Jantzen, Carini & Bini (1992); Mashhoon (2001); Rindler (2001); Mashhoon (2007); Costa & Herdeiro (2008); Costa & Natário (2014, 2021); Ruggiero (2021), and references therein. Actually, general relativistic gravitoelectromagnetism has nothing to do with electric charges and currents, implying a number of purely gravitational phenomena affecting orbiting test particles, precessing gyroscopes, moving clocks and atoms, and propagating electromagnetic waves (Braginsky, Caves & Thorne 1977; Dymnikova 1986; Tartaglia 2002; Ruggiero & Tartaglia 2002; Schäfer 2004, 2009; Stella & Possenti 2009). In particular, it turns out that matter-energy currents give rise to a “gravitomagnetic” component of the gravitational field encoded in the off-diagonal components g_{0i} , $i = 1, 2, 3$ of the spacetime metric tensor $g_{\mu\nu}$, $\mu, \nu = 0, 1, 2, 3$. To the first post-Newtonian (1pN) order, in the case of an isolated, slowly spinning body, the source of its gravitomagnetic field is just its spin angular momentum S which, among other things, induces a non-central, Lorentz-like acceleration on an orbiting test particle. It causes secular precessions of the orbit of the latter (Soffel 1989; Brumberg 1991; Soffel & Han 2019) which go by the

²See also <https://www.space.com/china-probes-jupiter-uranus-same-launch> on the Internet.

³For a recent overview of the Einstein’s theory of gravity, see, e.g., Debono & Smoot (2016), and references therein.

name of Lense-Thirring (LT) effect (Lense & Thirring 1918; Mashhoon, Hehl & Theiss 1984). Gravitomagnetism has been experimentally measured in a, so far, undisputed way only in the field of the spinning Earth with the dedicated GP-B spacecraft-based mission which measured the Pugh-Schiff precessions (Pugh 1959; Schiff 1960) of the axes of four gyroscopes carried onboard to a 19 per cent accuracy (Everitt et al. 2011). As per the LT orbital precessions, somewhat controversial attempts to measure them with the Earth’s artificial satellites of the LAGEOS type (Pearlman et al. 2019) and the Satellite Laser Ranging (SLR) technique (Coulot et al. 2011) are currently ongoing (Ciufolini et al. 2013; Renzetti 2013; Iorio, Ruggiero & Corda 2013); see Iorio et al. (2011) and references therein also for other proposed tests with natural and artificial bodies in the solar system. Recently, a successful detection of the gravitomagnetic orbital precessions in a tight astrophysical binary system made of a white dwarf and a pulsar was claimed (Venkatraman Krishnan et al. 2020), but also such a test subsequently raised concerns (Iorio 2020). Efforts for measuring the LT periastron precession of the double pulsar PSR J0737-3039A/B (Burgay et al. 2003; Lyne et al. 2004) in the next future are underway (Kehl et al. 2017; Hu et al. 2020).

Here, we investigate the possibility of measuring the gravitomagnetic LT orbital precessions of a putative Uranian orbiter, provisionally dubbed EURO (Elliptical Uranian Relativity Orbiter), independently of the competing ones due to the even and odd zonal harmonics J_ℓ , $\ell = 2, 3, 4, \dots$ of the planet’s gravity field, which are other physical parameters of great interest (Neuenschwander & Helled 2022). The peculiar obliquity of 98° of the Uranian spin axis (Bergstrahl, Miner & Matthews 1991; Hubbard 1997), whose origin is, at present, actively investigated (Rogoszinski & Hamilton 2021; Saillenfest et al. 2022), is instrumental for the achievement of such a goal. For the sake of clarity, the standard Keplerian orbital elements (Murray & Dermott 2000; Bertotti, Farinella & Vokrouhlický 2003; Kopeikin, Efroimsky & Kaplan 2011) are used to perform a sensitivity analysis, which however is not intended to replace future simulations of the actual observables (such as range-rate), including fitting parameters and a full covariance analysis.

The paper is organized as follows. In Section 2, the LT effect for an arbitrary orientation of the primary’s spin axis is reviewed, while the competing classical precessions induced by the quadrupole mass moment of the central body are treated in Section 3. Section 4 deals with the orbital geometry which better allows to separate the aforementioned relativistic and Newtonian effects each other. In Section 5, numerical values are given for a pair of specific wide and elliptical trajectories of EURO, and the range-rate is considered as well. The impact of the errors in the planetary spin axis orientation and in the orbital inclination on the classical precessions is examined. In Section 6, the conditions and the requirements for the implementation of the previously considered orbits are discussed. Section 7 summarizes our findings and offers our conclusions. Appendix A shows the details of the calculation of the classical orbital precessions due to the first seven zonal harmonics of the planet’s gravity field, while Appendix B is dedicated to the approximate analytical calculation of the range-rate shift of a spacecraft orbiting a distant planet. In Appendix C, some suggestions for properly naming the pericentre and the apocentre in the case of Uranus are offered.

2. The generalized Lense-Thirring orbital precessions

Let an isolated, massive rotating body orbited by a test particle be considered.

The generalized⁴ LT averaged rates of the inclination I of the orbital plane to the reference $\{x, y\}$ plane adopted, of the longitude of the ascending node Ω and of the argument of pericentre ω are (Iorio 2017)

$$\dot{I}^{\text{LT}} = \frac{2GS (\hat{\mathbf{k}} \cdot \hat{\mathbf{l}})}{c^2 a^3 (1 - e^2)^{3/2}}, \quad (3)$$

$$\dot{\Omega}^{\text{LT}} = \frac{2GS \csc I (\hat{\mathbf{k}} \cdot \hat{\mathbf{m}})}{c^2 a^3 (1 - e^2)^{3/2}}, \quad (4)$$

$$\dot{\omega}^{\text{LT}} = -\frac{2GS \hat{\mathbf{k}} \cdot (2\hat{\mathbf{h}} + \cot I \hat{\mathbf{m}})}{c^2 a^3 (1 - e^2)^{3/2}}; \quad (5)$$

for other derivations based on different parameterizations, see also Barker & O’Connell (1975); Damour & Schäfer (1988); Damour & Taylor (1992). In Equations (3)–(5), G is the Newtonian constant of gravitation, c is the speed of light in vacuum, $\hat{\mathbf{k}}$ is the spin axis of the central body so that $\mathbf{S} = S \hat{\mathbf{k}}$,

$$\hat{\mathbf{h}} = \{\sin I \sin \Omega, -\sin I \cos \Omega, \cos I\} \quad (6)$$

is the unit vector of the orbital angular momentum of the test particle (Soffel 1989; Brumberg 1991; Soffel & Han 2019),

$$\hat{\mathbf{l}} = \{\cos \Omega, \sin \Omega, 0\} \quad (7)$$

is the unit vector directed along the line of the nodes toward the ascending node (Soffel 1989; Brumberg 1991; Soffel & Han 2019),

$$\hat{\mathbf{m}} = \{-\cos I \sin \Omega, \cos I \cos \Omega, \sin I\} \quad (8)$$

is a unit vector lying in the orbital plane (Soffel 1989; Brumberg 1991; Soffel & Han 2019) such that $\hat{\mathbf{l}} \times \hat{\mathbf{m}} = \hat{\mathbf{h}}$, a is the semimajor axis, and e is the eccentricity.

Since the reference frame usually adopted for processing solar system’s spacecraft data is the ICRF (International Celestial Reference Frame) (Ma et al. 1998; Petit & Luzum 2010), whose

⁴The formulas obtained originally by Lense & Thirring (1918) and often reported in the literature (Soffel 1989; Brumberg 1991; Soffel & Han 2019) hold when the orientation of \mathbf{S} is known, so that it can be aligned with, say, the reference z axis of the coordinate system adopted; in such a case, the reference $\{x, y\}$ plane coincides with the body’s equatorial one.

reference plane, the Celestial Equator (CE), coincides with the Earth's equatorial plane at the reference epoch J2000, it is useful to parameterize $\hat{\mathbf{k}}$ in terms of the right ascension (RA) α and declination (DEC) δ of the planet's pole of rotation as

$$\hat{k}_x = \cos \delta \cos \alpha, \quad (9)$$

$$\hat{k}_y = \cos \delta \sin \alpha, \quad (10)$$

$$\hat{k}_z = \sin \delta. \quad (11)$$

By means of Equations (9)–(11), Equations (3)–(5) can be cast into the form

$$i^{\text{LT}} = \frac{2 G S \cos \delta \cos \eta}{c^2 a^3 (1 - e^2)^{3/2}}, \quad (12)$$

$$\dot{\Omega}^{\text{LT}} = \frac{2 G S (\sin \delta + \cos \delta \cot I \sin \eta)}{c^2 a^3 (1 - e^2)^{3/2}}, \quad (13)$$

$$\dot{\omega}^{\text{LT}} = -\frac{2 G S [3 \cos I \sin \delta + \cos \delta (\csc I - 3 \sin I) \sin \eta]}{c^2 a^3 (1 - e^2)^{3/2}}, \quad (14)$$

where

$$\eta \doteq \alpha - \Omega \quad (15)$$

is the planetary spin's RA reckoned from the line of the nodes. Note that, for

$$\delta = 90^\circ, \quad (16)$$

the usual formulas by Lense & Thirring (1918),

$$i^{\text{LT}} = 0, \quad (17)$$

$$\dot{\Omega}^{\text{LT}} = \frac{2 G S}{c^2 a^3 (1 - e^2)^{3/2}}, \quad (18)$$

$$\dot{\omega}^{\text{LT}} = -\frac{6 G S \cos I}{c^2 a^3 (1 - e^2)^{3/2}}, \quad (19)$$

valid, e.g., for an Earth's satellite, are restored.

In the case of Uranus, the general formulas of Equations (3)–(5), or Equations (12)–(14), are required since the orientation of its spin axis with respect to the ICRF is given by (Jacobson 2014)

$$\alpha_{\mathfrak{S}} = 77.310^\circ, \quad (20)$$

$$\delta_{\mathfrak{S}} = 15.172^\circ. \quad (21)$$

Thus,

$$\hat{k}_x^{\mathfrak{S}} = 0.212, \quad (22)$$

$$\hat{k}_y^{\mathfrak{S}} = 0.941, \quad (23)$$

$$\hat{k}_z^{\mathfrak{S}} = 0.262; \quad (24)$$

the spin of Uranus mainly lies in the CE. As a consequences, Equations (17)–(19) cannot be used in the present case.

3. The orbital precessions induced by J_2

The first even zonal harmonic coefficient J_2 of the multipolar expansion of the classical part of the non-spherical planetary gravitational potential $U(\mathbf{r})$ induces the largest orbital precessions among those due to the deviations of U from spherical symmetry (Capderou 2005); they act as major systematic bias with respect to the relativistic rates of Equations (3)–(5).

For an arbitrary⁵ orientation of $\hat{\mathbf{k}}$ in space, the oblateness-driven averaged rates are (Iorio 2017)

$$\dot{I}^{J_2} = -\frac{3}{2} n_b J_2 \left(\frac{R}{p}\right)^2 (\hat{\mathbf{k}} \cdot \hat{\mathbf{l}}) (\hat{\mathbf{k}} \cdot \hat{\mathbf{h}}), \quad (25)$$

$$\dot{\Omega}^{J_2} = -\frac{3}{2} n_b J_2 \left(\frac{R}{p}\right)^2 \csc I (\hat{\mathbf{k}} \cdot \hat{\mathbf{m}}) (\hat{\mathbf{k}} \cdot \hat{\mathbf{h}}), \quad (26)$$

$$\dot{\omega}^{J_2} = \frac{3}{4} n_b J_2 \left(\frac{R}{p}\right)^2 \left\{ 2 - 3 \left[(\hat{\mathbf{k}} \cdot \hat{\mathbf{l}})^2 + (\hat{\mathbf{k}} \cdot \hat{\mathbf{m}})^2 \right] + 2 \cot I (\hat{\mathbf{k}} \cdot \hat{\mathbf{m}}) (\hat{\mathbf{k}} \cdot \hat{\mathbf{h}}) \right\}, \quad (27)$$

⁵The same considerations as in footnote 4 hold here for the oblateness-induced orbital precessions. Their expressions for $\hat{\mathbf{k}}$ aligned with the reference z axis can be found, e.g., in Capderou (2005); they are reported in Equations (34)–(36).

where

$$n_b \doteq \sqrt{\frac{GM}{a^3}} \quad (28)$$

is the Keplerian mean motion, and

$$p \doteq a (1 - e^2) \quad (29)$$

is the orbital semilatus rectum.

By means of Equations (9)–(11), Equations (25)–(27) can be suitably expressed as

$$\dot{I}^{J_2} = \frac{3}{2} n_b J_2 \left(\frac{R}{p}\right)^2 [\cos \delta \cos \eta (-\cos I \sin \delta + \cos \delta \sin I \sin \eta)], \quad (30)$$

$$\dot{\Omega}^{J_2} = -\frac{3}{2} n_b J_2 \left(\frac{R}{p}\right)^2 \csc I (\sin I \sin \delta + \cos I \cos \delta \sin \eta) (\cos I \sin \delta - \cos \delta \sin I \sin \eta), \quad (31)$$

$$\begin{aligned} \dot{\omega}^{J_2} = & -\frac{3}{8} n_b J_2 \left(\frac{R}{p}\right)^2 [-4 + (1 - 5 \cos 2I) \sin^2 \delta + (3 - 5 \cos 2I) \cot I \sin 2\delta \sin \eta + \\ & + 2 \cos^2 \delta (3 \cos^2 \eta + 5 \cos^2 I \sin^2 \eta)]. \end{aligned} \quad (32)$$

Note that, for

$$\delta = 90^\circ, \quad (33)$$

Equations (30)–(32) reduce to the standard formulas (Capderou 2005)

$$\dot{I}^{J_2} = 0, \quad (34)$$

$$\dot{\Omega}^{J_2} = -\frac{3}{2} n_b J_2 \left(\frac{R}{p}\right)^2 \cos I, \quad (35)$$

$$\dot{\omega}^{J_2} = \frac{3}{8} n_b J_2 \left(\frac{R}{p}\right)^2 (3 + 5 \cos 2I). \quad (36)$$

valid, e.g., for an Earth's satellite.

The details of the calculation of the precessions induced by the zonal harmonics J_ℓ of any degree ℓ can be found in Appendix A.

4. Choosing the most suitable orbital geometry

From Equations (3)–(5) and Equations (25)–(27), it turns out that, if

$$\hat{\mathbf{k}} \cdot \hat{\mathbf{h}} = 0, \quad (37)$$

$$\hat{\mathbf{k}} \cdot \hat{\mathbf{m}} \neq 0, \quad (38)$$

$$\hat{\mathbf{k}} \cdot \hat{\mathbf{l}} \neq 0, \quad (39)$$

i.e., if the body’s spin axis lies in the orbital plane of the test particle somewhere between the line of the nodes and the direction perpendicular to the latter, the J_2 -induced shifts of I (Equation (25)) and Ω (Equation (26)) vanish, contrary to the corresponding gravitomagnetic ones of Equations (3)–(4). Then, the relativistic node and inclination precessions would not be biased at all by the classical disturbances due to the body’s oblateness. The condition of Equation (37), corresponding to a polar orbit, is usually selected in order to fulfil some of the planetological scopes of most of the proposed Uranian missions (see, e.g., Simon, Nimmo & Anderson (2021); Girija (2023)).

By means of Equations (6)–(11), the conditions of Equations (37)–(39) are equivalent to

$$\tan I = \csc \eta \tan \delta, \quad (40)$$

$$\tan I \neq -\sin \eta \cot \delta, \quad (41)$$

$$\cos \eta \cos \delta \neq 0. \quad (42)$$

In the case of Uranus, according to Equation (21), it is

$$\sin \delta_{\hat{\circ}} = 0.262 \neq 0, \quad (43)$$

$$\cos \delta_{\hat{\circ}} = 0.965 \neq 0. \quad (44)$$

Thus, for EURO, Equations (40)–(42) can be simultaneously fulfilled if the planetary spin’s RA relative to the node

$$\eta \neq 90^\circ. \quad (45)$$

In particular, if one chooses

$$\eta = 0, \quad (46)$$

then, from Equations (40)–(42), it turns out that

$$I = 90^\circ, \quad (47)$$

implying that the gravitomagnetic pericentre precession of Equation (14) vanishes, contrary to the classical one of Equation (32). Indeed, Equations (12)–(13) and Equation (32), calculated with Equations (46)–(47), reduce to the following secular rates

$$\dot{I}^{\text{LT}} = \frac{2 G S \cos \delta}{c^2 a^3 (1 - e^2)^{3/2}}, \quad (48)$$

$$\dot{\Omega}^{\text{LT}} = \frac{2 G S \sin \delta}{c^2 a^3 (1 - e^2)^{3/2}}, \quad (49)$$

$$\dot{\omega}^{J_2} = -\frac{3}{4} n_b J_2 \left(\frac{R}{p} \right)^2. \quad (50)$$

Furthermore, as shown in Appendix A, the averaged classical rates of I and Ω vanish also for the even and odd zonals of degree $\ell > 2$, contrary to the pericentre which turns out to be impacted by the odd zonals as well. Thus, in principle, one could separate the general relativistic signatures of I and Ω from the Newtonian ones of ω due to J_ℓ , $\ell = 2, 3, 4, \dots$ which could be used to simultaneously determine the multipolar field of Uranus without any a-priori “imprinting” due to its 1pN gravitomagnetic field, and vice-versa: S and J_ℓ , $\ell = 2, 3, 4, \dots$ could, then, be measured independently of each other. It would be important since, although there is no strict one-to-one correspondence between $J_2^{\hat{\circ}}$ and the Uranus’ MoI (Neuenschwander & Helled 2022, Sect. 3.3), there is a rather strong correlation between the other Uranian multipolar coefficients J_4 , J_6 , J_8 , and the MoI (Neuenschwander & Helled 2022). General relativity would, instead, imprint the classical pericentre precessions through the mismodelled part of its “gravitoelectric” 1pN counterpart given by (Soffel 1989; Brumberg 1991; Soffel & Han 2019)

$$\dot{\omega}^{\text{GE}} = \left(\frac{2 + 2\gamma - \beta}{3} \right) \frac{3 n_b \mu}{c^2 p}, \quad (51)$$

where γ , β are the parameterized post-Newtonian (PPN) parameters (Will & Nordtvedt 1972; Will 2018) which are equal to unity in general relativity.

5. The case of a polar, highly eccentric Uranian orbiter

By calculating Equation (1) with (Neuenschwander & Helled 2022, Tab. 1)

$$P_{\hat{\circ}} = 17.24 \text{ hr} \quad (52)$$

and (Neuenschwander & Helled 2022, Tab. 2)

$$\mathcal{J}_{\hat{\circ}} = 0.22594, \quad (53)$$

along with the reference radius for the Uranian zonal harmonics (French et al. 1988)

$$R_{\hat{\circ}} = 25\,559 \text{ km} \quad (54)$$

and⁶ (Jacobson 2014)

$$\mu_{\hat{\circ}} = 5\,794\,556.4 \times 10^9 \text{ m}^3 \text{ s}^{-2}, \quad (55)$$

a reasonable guess for the Uranian spin angular momentum may be

$$S_{\hat{\circ}} \simeq 1.29 \times 10^{36} \text{ kg m}^2 \text{ s}^{-1}. \quad (56)$$

It turns out that calculating Equation (1) with the other values for $P_{\hat{\circ}}$ and $\mathcal{J}_{\hat{\circ}}$ in Neuenschwander & Helled (2022, Tab. 1-2) yields a $\simeq 1$ per cent uncertainty in the theoretically predicted value of $S_{\hat{\circ}}$.

As far as the shape and the size of the spacecraft's path are concerned, wide and highly elliptical orbits are usually adopted for the orbital phase of several proposed missions. Just as an example for Uranus, a $4\,000 \times 550\,000$ km orbit was recently proposed by Girija (2023) in several simulations.

Here, a lower and smaller $2\,000 \times 100\,000$ km path, corresponding to

$$a = 76\,559 \text{ km}, e = 0.6400, P_b = 15.3 \text{ hr}, \quad (57)$$

where P_b is the orbital period of the probe, will be examined. Figure 1 depicts such kind of orbit (purple) oriented according to Equations (46)–(47).

A further scenario, shown in Figure 2, encompasses a less eccentric orbit with apocentre height $h_{\text{apo}} = 10\,000$ km, corresponding to

$$a = 31\,559 \text{ km}, e = 0.1267, P_b = 4.06 \text{ hr}. \quad (58)$$

For details on the practical implementation of such orbital geometries, see Section 6.

5.1. The orbital precessions

By assuming (Jacobson 2014)

$$J_2^{\hat{\circ}} (\times 10^6) = 3\,510.7, \quad (59)$$

⁶The values of Equations (54)–(55) are reported also in Neuenschwander & Helled (2022, Tab. 1)

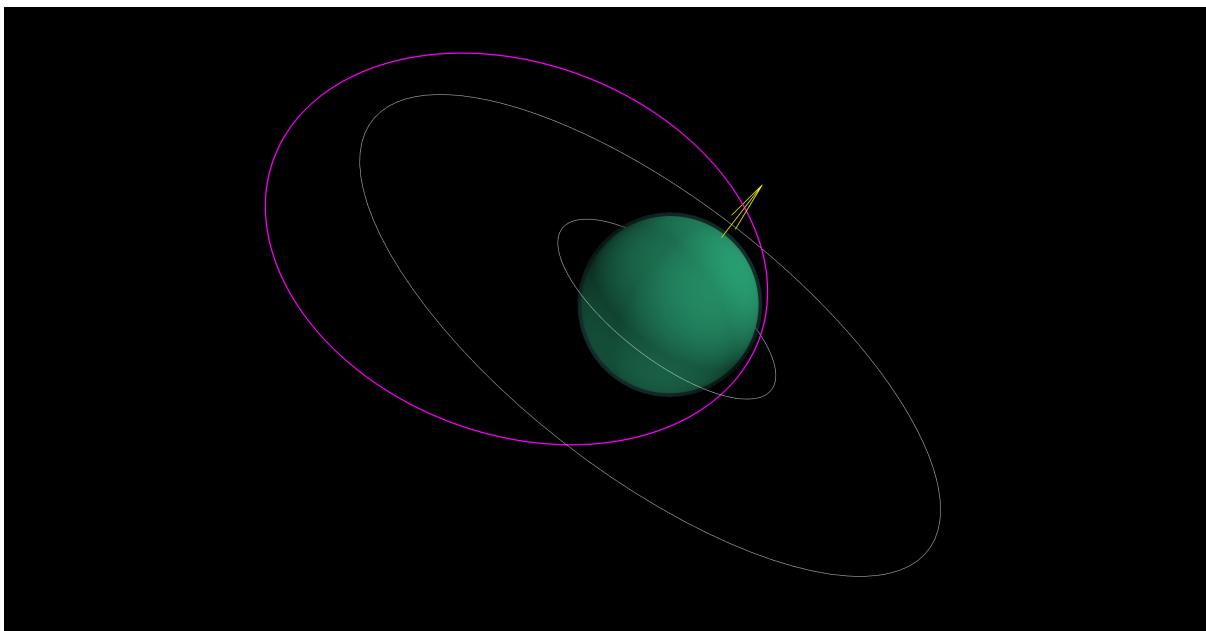


Fig. 1.— Orbital geometry of EURO for a $2\,000 \times 100\,000$ km orbit (purple) oriented with respect to the ICRF according to Equations (46)–(47). The Uranian spin axis, in yellow, is oriented as per Equations (20)–(21) with respect to the CE. The white circles represent the innermost (1986U2R/ ζ) and outermost (μ) rings of Uranus, respectively.

Equations (48)–(50) and⁷ Equation (51), calculated with the orbital parameters of Equation (57), yield

$$\dot{I}^{\text{LT}} \simeq 59.5 \text{ mas yr}^{-1}, \quad (60)$$

$$\dot{\Omega}^{\text{LT}} \simeq 16.1 \text{ mas yr}^{-1}, \quad (61)$$

$$\dot{\omega}^{J_2} = -173.0^\circ \text{ yr}^{-1}, \quad (62)$$

$$\dot{\omega}^{\text{GE}} = 3.2 \text{ arcsec yr}^{-1}, \quad (63)$$

where mas yr^{-1} and arcsec yr^{-1} stand for milliarcseconds per year and arcseconds per year, respectively.

⁷The gravitoelectric pericentre precession was computed for $\gamma = \beta = 1$.

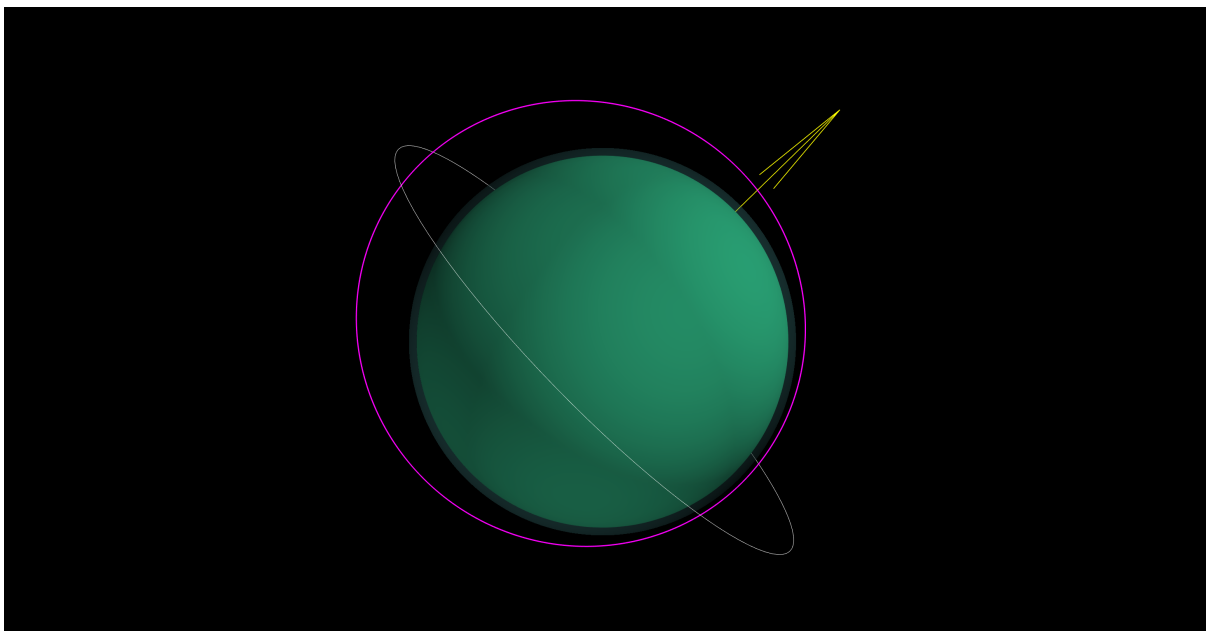


Fig. 2.— Orbital geometry of EURO for a $2\,000 \times 10\,000$ km orbit oriented with respect to the ICRF according to Equations (46)–(47). The Uranian spin axis, in yellow, is oriented as per Equations (20)–(21) with respect to the CE. The white circles represent the innermost (1986U2R/ ζ) and outermost (μ) rings of Uranus, respectively.

The $2\,000 \times 10\,000$ km orbit of Equation (58) yields

$$\dot{I}^{\text{LT}} \simeq 394.6 \text{ mas yr}^{-1}, \quad (64)$$

$$\dot{\Omega}^{\text{LT}} \simeq 107.0 \text{ mas yr}^{-1}, \quad (65)$$

$$\dot{\omega}^{J_2} = -1\,384.9^\circ \text{ yr}^{-1}, \quad (66)$$

$$\dot{\omega}^{\text{GE}} = 17.4 \text{ arcsec yr}^{-1}, \quad (67)$$

Figure 3 displays the nominal orbital precessions as per Equations (48)–(51) along with the semimajor axis a , in km, and the eccentricity e as functions of h_{apo} , ranging from 2 000 to 100 000 km, for a fixed value of the pericentre height $h_{\text{peri}} = 2\,000$ km.

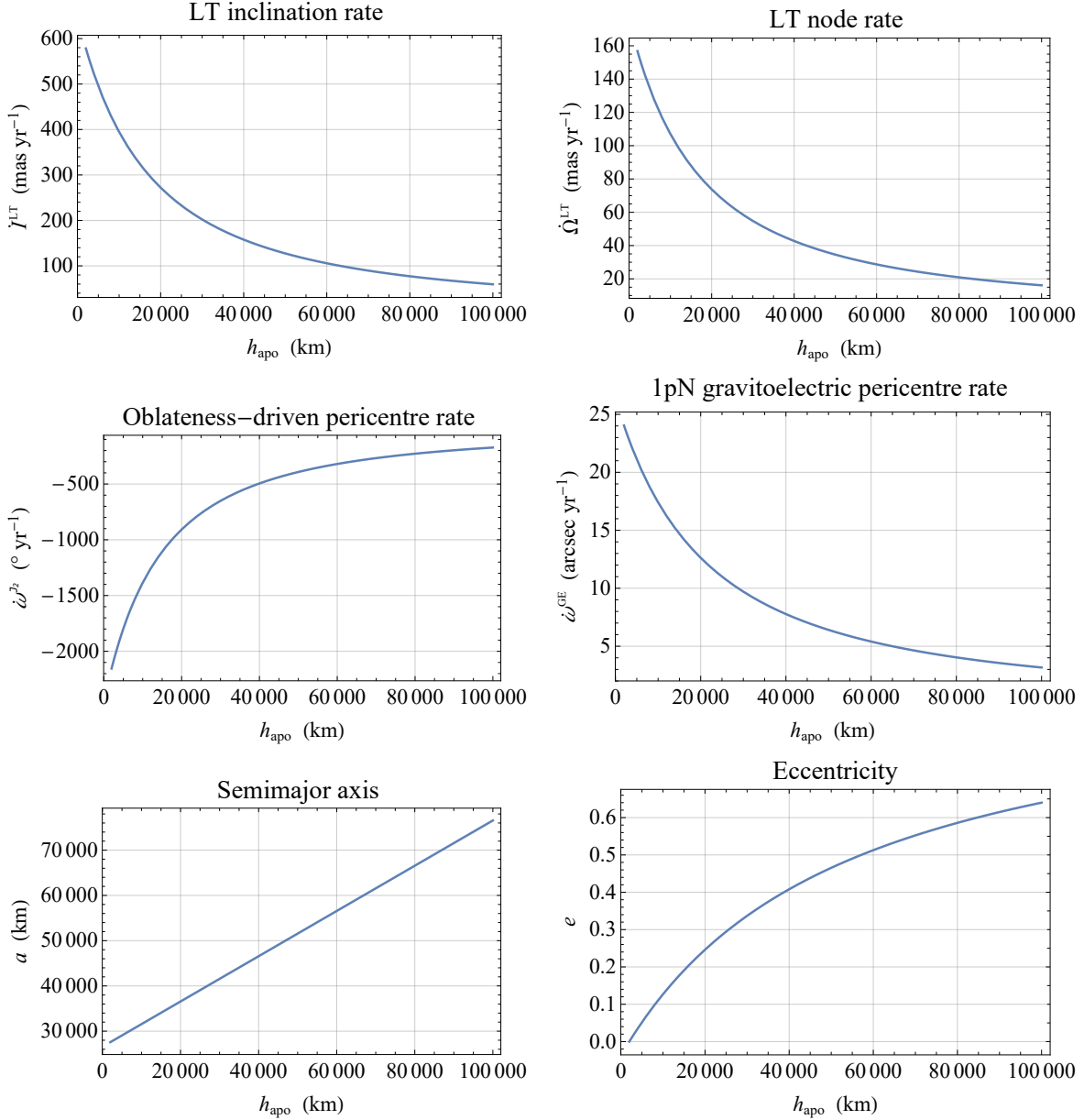


Fig. 3.— Upper row: LT precessions of the inclination I (left panel) and of the node Ω (right panel), in mas yr⁻¹, calculated from Equations (48)–(49) as functions of h_{apo} , in km, for a fixed value of $h_{\text{peri}} = 2\,000$ km. For $\delta_{\hat{\delta}}$ and $S_{\hat{\delta}}$, Equation (21) and Equation (56) were adopted, respectively. Middle row: oblateness-driven (left panel) and 1pN gravitoelectric (right panel) precessions of the pericentre ω , in degrees per year (° yr⁻¹) and arcseconds per year (arcsec yr⁻¹), respectively, calculated from Equations (50)–(51) as functions of h_{apo} , in km, for a fixed value of $h_{\text{peri}} = 2\,000$ km. For $R_{\hat{\delta}}$ and $J_2^{\hat{\delta}}$, Equation (54) and Equation (59) were adopted, respectively. Lower row: semimajor axis a , in km, (left panel) and eccentricity e (right panel) calculated for as functions of h_{apo} , in km, for a fixed value of $h_{\text{peri}} = 2\,000$ km.

About the “imprinting” of the mismodelling in the 1pN gravitoelectric pericentre precession on the classical one, from Equation (51) it turns out that, in principle, it is mainly due to the errors in the PPN parameters γ and β , currently known at the $\approx 10^{-5}$ accuracy level (Bertotti, Iess & Tortora 2003; Pitjeva & Pitjev 2014; Fienga et al. 2015; Park et al. 2017; Genova et al. 2018). Instead, the error in the Uranian gravitational parameter $\mu_{\hat{\delta}}$ would be of less concern. Indeed, according to Jacobson (2014), its current relative uncertainty amounts to just

$$\frac{\sigma_{\mu_{\hat{\delta}}}}{\mu_{\hat{\delta}}} = 7 \times 10^{-7}. \quad (68)$$

However, Equations (62)–(63) and the pictures in the middle row of Figure 3 show that the issue of the 1pN bias on the determination of $J_2^{\hat{\delta}}$ is negligible; suffice it to say that the current relative uncertainty in $J_2^{\hat{\delta}}$ is 2×10^{-4} , as per Table 12 of Jacobson (2014).

5.1.1. *The impact of the uncertainty in the pole of Uranus*

Here, the consequences of the current level of uncertainty in our knowledge of the orientation of the Uranian spin axis on the otherwise idealized situation outlined in Section 4 is examined.

At present, the pole of Uranus is known to an accuracy of (Jacobson 2014)

$$\sigma_{\alpha_{\hat{\delta}}} = 0.002^\circ = 7.2 \text{ arcsec}, \quad (69)$$

$$\sigma_{\delta_{\hat{\delta}}} = 0.002^\circ = 7.2 \text{ arcsec}. \quad (70)$$

Such a somewhat modest accuracy is due to the present lack of dedicated, in-situ missions, contrary to the case, of, e.g., Cassini at Saturn (Spilker 2019); for the Kronian spin axis, Jacobson (2022) recently obtained

$$\sigma_{\alpha_{\hat{h}}} \simeq 0.0001^\circ = 0.36 \text{ arcsec}, \quad (71)$$

$$\sigma_{\delta_{\hat{h}}} \simeq 0.00003^\circ = 0.1 \text{ arcsec}. \quad (72)$$

The mismodelled quadrupole-induced orbital precessions due to the uncertainty in the primary’s spin axis can be analytically evaluated as

$$\sigma_{\kappa^{J_2}} = \sqrt{\left(\frac{\partial \kappa^{J_2}}{\partial \alpha}\right)^2 \sigma_{\alpha}^2 + \left(\frac{\partial \kappa^{J_2}}{\partial \delta}\right)^2 \sigma_{\delta}^2}, \quad \kappa = I, \Omega, \quad (73)$$

starting from Equations (30)–(31).

For the $2\,000 \times 100\,000$ km orbit of Equation (57), Equation (73), applied to Equations (30)–(31) with Equations (46)–(47) and Equations (69)–(70), yields

$$\sigma_{j^{\prime 2}} = 40\,502 \text{ mas yr}^{-1}, \quad (74)$$

$$\sigma_{\dot{\Omega}^{\prime 2}} = 10\,983 \text{ mas yr}^{-1}, \quad (75)$$

which are about 3 orders of magnitude larger than the nominal LT rates of Equations (60)–(61).

In the case of the less eccentric $2\,000 \times 10\,000$ km orbit of Equation (58), one has

$$\sigma_{j^{\prime 2}} = 324\,220 \text{ mas yr}^{-1}, \quad (76)$$

$$\sigma_{\dot{\Omega}^{\prime 2}} = 87\,918 \text{ mas yr}^{-1}, \quad (77)$$

which are $\simeq 2 - 3$ orders of magnitude larger than Equations (64)–(65).

Thus, $\alpha_{\hat{\delta}} \delta_{\hat{\delta}}$ should be determined with an error as little as

$$\sigma_{\alpha_{\hat{\delta}}} \simeq \sigma_{\delta_{\hat{\delta}}} \simeq 0.1 - 1 \text{ mas}. \quad (78)$$

A further potential challenge is represented by the uncertainty σ_I in the orbital inclination I to the CE; applying Equation (73) to such a potentially major source of systematic bias yields that I would need to be determined with an accuracy as good as

$$\sigma_I \simeq 1 - 10 \text{ mas}. \quad (79)$$

5.2. The range-rate and rate shifts

One of the most accurately measured observable in a spacecraft-based mission to a planet P is the Earth-probe range-rate $\dot{\rho}$. As an example, the two-way Ka-band Doppler range-rate measurements of the spacecraft Juno (Bolton 2018), currently orbiting Jupiter, are accurate to a $\simeq 1 \times 10^{-2}$ millimetre per second (mm s^{-1}) level over 60 s after having processed data covering up to the middle of its prime mission (Durante et al. 2020).

For the computational strategy to recover the shift $\Delta\dot{\rho}$ of the dynamical part of the range-rate due to the planetocentric orbital motion affected by a perturbing acceleration, see Appendix B.

In the case of the LT effect, the gravitomagnetic acceleration \mathbf{A}_{LT} can be found, e.g., in Soffel (1989); Petit & Luzum (2010); Soffel & Han (2019), and its radial, transverse and out-of-plane components in terms of the unit vectors $\hat{\mathbf{l}}, \hat{\mathbf{m}}, \hat{\mathbf{h}}$ are explicitly displayed in Iorio (2017). The

resulting relevant gravitomagnetic shifts, calculated for the particular orbital geometry of Equations (46)–(47), turn out to be

$$\Delta a^{\text{LT}}(f) = 0, \quad (80)$$

$$\Delta e^{\text{LT}}(f) = 0, \quad (81)$$

$$\begin{aligned} \Delta I^{\text{LT}}(f) = & \frac{GS}{2c^2 n_b a^3 (1-e^2)^{3/2}} \{4(f-f_0) \cos \delta + 4 \cos(f+f_0-\delta+2\omega) \sin(f-f_0) + \\ & + e [3 \sin(f-\delta) - 3 \sin(f_0-\delta) + \sin(f+\delta) - \sin(f_0+\delta) + \sin(f-\delta+2\omega) + \\ & + \sin(3f-\delta+2\omega) - 2 \cos f_0 \sin(2f_0-\delta+2\omega)]\}, \quad (82) \end{aligned}$$

$$\begin{aligned} \Delta \Omega^{\text{LT}}(f) = & -\frac{GS}{2c^2 n_b a^3 (1-e^2)^{3/2}} \{2 \cos(2f-\delta+2\omega) - 2 \cos(2f_0-\delta+2\omega) + \\ & + e [-3 \cos(f-\delta) + 3 \cos(f_0-\delta) + \cos(f+\delta) - \cos(f_0+\delta) + \cos(f-\delta+2\omega) + \\ & + \cos(3f-\delta+2\omega) - 2 \cos f_0 \cos(2f_0-\delta+2\omega)] + 4(-f+f_0) \sin \delta\}, \quad (83) \end{aligned}$$

$$\Delta \omega^{\text{LT}}(f) = 0, \quad (84)$$

$$\Delta \mathcal{M}^{\text{LT}}(f) = 0, \quad (85)$$

where f is the true anomaly reckoning the instantaneous position of the test particle along its orbit, f_0 is the value of the true anomaly at some initial instant t_0 , and \mathcal{M} is the mean anomaly. Thus, for the LT perturbations of the radial (R), transverse (T) and out-of-plane (N) components of the velocity one has

$$\Delta v_R^{\text{LT}}(f) = 0, \quad (86)$$

$$\Delta v_T^{\text{LT}}(f) = 0, \quad (87)$$

$$\Delta v_N^{\text{LT}}(f) = \frac{GS}{2c^2 a^2 (1-e^2)^2} (4e(f-f_0) \cos(\delta-\omega) + 4(f-f_0) \cos(f-\delta+\omega) +$$

$$\begin{aligned}
& + 4 \cos (f_0 - \delta + \omega) \sin (f - f_0) + e \{ \sin (f - 3f_0 + \delta - \omega) + \sin (f - f_0 + \delta - \omega) + \\
& + 6 \sin (2f - \delta + \omega) + \sin (f - f_0 - \delta + \omega) - 3 \sin (f + f_0 - \delta + \omega) - \\
& - 2 \sin (2f_0 - \delta + \omega) + e [\sin (f + \delta - \omega) - \sin (f_0 + \delta - \omega) + \\
& + 4 \sin (f - \delta + \omega) + \sin (3f - \delta + \omega) - 4 \sin (f_0 - \delta + \omega) - \sin (3f_0 - \delta + \omega)] \}. \quad (88)
\end{aligned}$$

Inserting Equations (86)–(88) in Equation (B.23) allows to obtain the instantaneous LT range-rate shift;

$$\begin{aligned}
\Delta \dot{\rho}^{\text{LT}}(f) = & -\frac{G S \cos \chi \sin (\alpha - \phi)}{2 c^2 a^2 (1 - e^2)^2} (4 e (f - f_0) \cos (\delta - \omega) + 4 (f - f_0) \cos (f - \delta + \omega) + \\
& + 4 \cos (f_0 - \delta + \omega) \sin (f - f_0) + e \{ \sin (f - 3f_0 + \delta - \omega) + \sin (f - f_0 + \delta - \omega) + \\
& + 6 \sin (2f - \delta + \omega) + \sin (f - f_0 - \delta + \omega) - 3 \sin (f + f_0 - \delta + \omega) - \\
& - 2 \sin (2f_0 - \delta + \omega) + e [\sin (f + \delta - \omega) - \sin (f_0 + \delta - \omega) + \\
& + 4 \sin (f - \delta + \omega) + \sin (3f - \delta + \omega) - 4 \sin (f_0 - \delta + \omega) - \sin (3f_0 - \delta + \omega)] \}), \quad (89)
\end{aligned}$$

where ϕ, χ are the RA and DEC of the planet, respectively.

After having averaged Equation (89) over one orbital revolution as

$$\langle \Delta \dot{\rho}^{\text{LT}} \rangle = \frac{n_b}{2\pi} \int_{f_0}^{f_0+2\pi} \Delta \dot{\rho}^{\text{LT}}(f) \frac{dt}{df} df, \quad (90)$$

and considering Equation (A.6), one finally gets for the net gravitomagnetic range-rate shift per orbit

$$\langle \Delta \dot{\rho}^{\text{LT}} \rangle = -\frac{2 G S \cos \chi \sin (\alpha - \phi) \sin (u_0 - \delta)}{c^2 a^2 \sqrt{1 - e^2} (1 + e \cos f_0)}. \quad (91)$$

The RA $\phi_{\text{♁}}$ and DEC $\chi_{\text{♁}}$ of Uranus, retrieved through the web interface HORIZONS maintained by the NASA Jet Propulsion Laboratory (JPL) for the epoch, say, 13 December 2032, are

$$\phi_{\text{♁}} = 89.455^\circ, \quad (92)$$

$$\chi_{\text{♁}} = 23.6497^\circ. \quad (93)$$

Equation (91), calculated with Equation (20), Equations (56)–(57) and Equations (92)–(93), yields

$$\langle \Delta \dot{\rho}^{\text{LT}} \rangle \left[\frac{1 + e \cos f_0}{\sin(u_0 - \delta)} \right] = - \frac{2 G S_{\delta} \cos \chi_{\delta} \sin(\alpha_{\delta} - \phi_{\delta})}{c^2 a^2 \sqrt{1 - e^2}} = 8 \times 10^{-5} \text{ mm s}^{-1}. \quad (94)$$

By selecting

$$f_0 = 180^\circ, \quad (95)$$

$$\omega = \delta_{\delta} - 90^\circ, \quad (96)$$

it is possible to maximize Equation (94), thus getting

$$\langle \Delta \dot{\rho}^{\text{LT}} \rangle = - \frac{2 G S_{\delta} \cos \chi_{\delta} \sin(\alpha_{\delta} - \phi_{\delta})}{c^2 a^2 \sqrt{1 - e^2} (1 - e)} = 2 \times 10^{-4} \text{ mm s}^{-1}. \quad (97)$$

Figure 4 plots Equation (97), in mm s^{-1} , as a function of the apocenter height h_{apo} , ranging from 2 000 to 100 000 km, for a fixed value of the pericentre height $h_{\text{peri}} = 2\,000$ km.

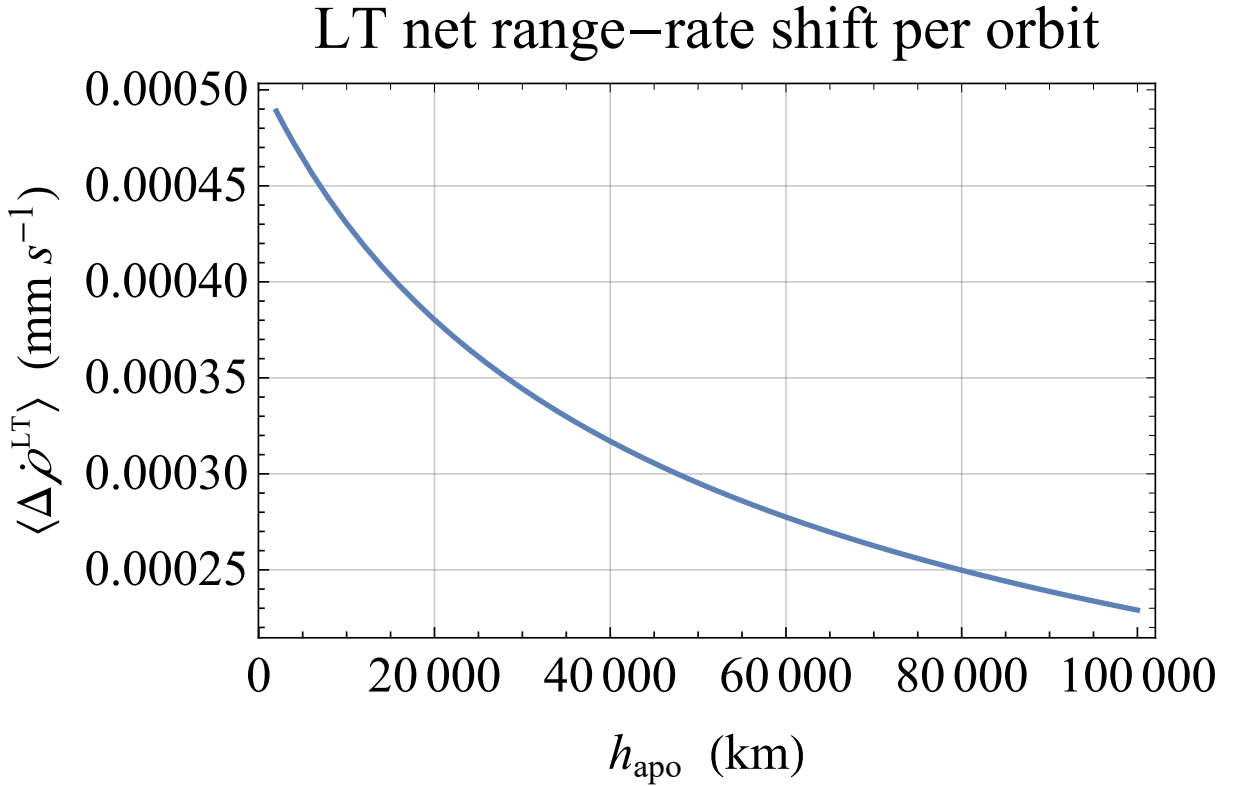


Fig. 4.— LT net shift per orbit $\langle \Delta \dot{\rho}^{\text{LT}} \rangle$, in mm s^{-1} , of the range-rate of EURO calculated from Equation(97) as a function of h_{apo} , in km, for a fixed value of $h_{\text{peri}} = 2000$ km. For $\alpha_{\hat{\delta}}$, $S_{\hat{\delta}}$, $\phi_{\hat{\delta}}$, $\chi_{\hat{\delta}}$, Equation (20), Equation (56), and Equations (92)–(93) were adopted, respectively.

It turns out that an apocentre height $h_{\text{apo}} \simeq 50\,000$ km allows to reach the $\simeq 3 \times 10^{-4}$ mm s⁻¹ level; for $h_{\text{apo}} = 10\,000$ km, the LT net range-rate shift is of the order of $\simeq 4 \times 10^{-4}$ mm s⁻¹.

Figure 5 depicts the instantaneous LT range-rate shift $\Delta\dot{\rho}^{\text{LT}}(t)$ during a single passage at the pericentre six hours long for the orbital configuration of Equation (57) and Equations (95)–(96). To this end, we expressed $\Delta\dot{\rho}^{\text{LT}}(f)$ from Equation (89) as a function of time by switching from f to time t through \mathcal{M} according to Brouwer & Clemence (1961)

$$f(t) = \mathcal{M}(t) + 2 \sum_{s=1}^{s_{\text{max}}} \frac{1}{s} \left\{ J_s(s e) + \sum_{j=1}^{j_{\text{max}}} \lambda^j [J_{s-j}(s e) + J_{s+j}(s e)] \right\} \sin(s\mathcal{M}(t)), \quad (98)$$

where

$$\mathcal{M}(t) = \mathcal{M}_0 + n_b (t - t_0), \quad (99)$$

$$\lambda = \frac{1 - \sqrt{1 - e^2}}{e}, \quad (100)$$

\mathcal{M}_0 is the mean anomaly at the initial epoch t_0 , and $J_k(s e)$ is the Bessel function of the first kind of order k . The initial instant t_0 corresponds to the passage at apocentre, as per Equation (95), so that

$$\mathcal{M}_0 = 180^\circ; \quad (101)$$

the pericentre is reached after half a orbital period.

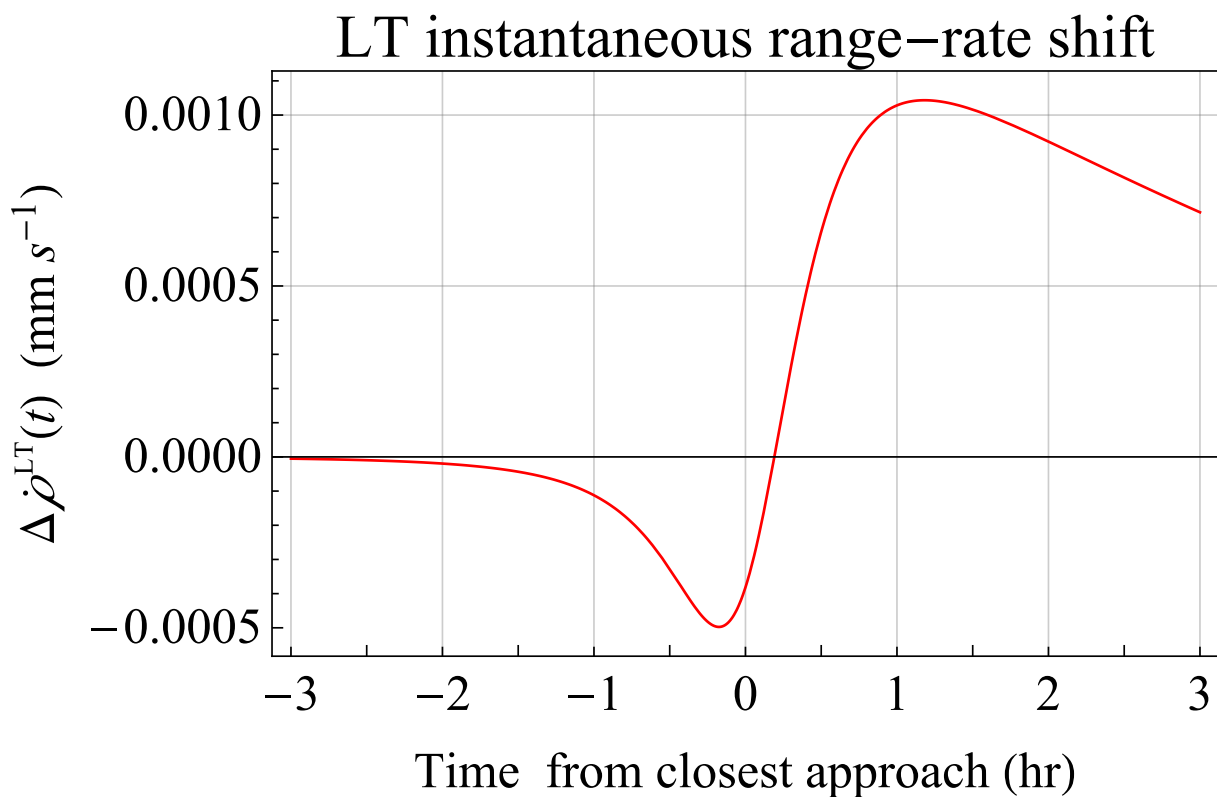


Fig. 5.— LT instantaneous shift $\Delta\dot{\rho}^{\text{LT}}(t)$, in mm s^{-1} , of the range-rate of EURO calculated from Equation (89) with Equation (57), corresponding to a $2\,000 \times 100\,000$ km orbit, and Equations (95)–(96) as a function of time t , according to Equation (98) for $s_{\text{max}} = j_{\text{max}} = 55$, during a passage 6 hours long centered at the pericentre. For $\alpha_{\text{♁}}$, $\delta_{\text{♁}}$, $S_{\text{♁}}$, $\phi_{\text{♁}}$, $\chi_{\text{♁}}$, Equations (20)–(21), Equation (56) and Equations (92)–(93), were adopted, respectively.

It can be noted that the peak-to-peak amplitude of the signal amounts to $\approx 1.5 \times 10^{-3} \text{ mm s}^{-1}$. Such figures are challenging if compared with the $\approx 10^{-2} \text{ mm s}^{-1}$ accuracy level of Juno.

6. Orbital configurations and requirements

Elliptical orbits are generally preferred in mission design, since they allow to greatly reduce the amount of propellant needed to impart the large change ΔV in speed required to finally insert the spacecraft in an circular, low trajectory (Hughes 2016). Moreover, it is also mandatory to avoid that the more or less energetic particles circling in the radiation belts around the giant planets (Schubert & Soderlund 2011; Masters, Ioannou & Rayns 2022) damage the instrumentation of the spacecraft, which would likely happen if the latter steadily moved at the same (small) distance from the planet in a circular, low orbit. Another drawback of an (almost) circular orbit is that the spacecraft would go behind Uranus every few hours, making, thus, difficult to communicate with the Earth. Another issue is that low orbits must avoid the Uranian ring system. Should the probe move completely inside the rings, the extended Uranian atmosphere would cause its orbit to quickly decay. Moreover, there would exist a significant risk of frequent ring plane crossing.

Here, it is shown how the technique of aerocapture (Cruz 1979; Leszczynski 1998; Spilker et al. 2019; Saikia et al. 2021; Girija et al. 2022) allows to insert a larger orbiter into an elliptical $2\,000 \times 100\,000 \text{ km}$ orbit, and a small secondary satellite into a closer and less elliptical $2\,000 \times 10\,000 \text{ km}$ orbit at Uranus; the orbital effects of interest for such orbital geometries were studied in Section 5. As shown by Equation (57) and Equation (58), the resulting orbital periods are relatively short, if compared to Juno or Cassini Grand Finale orbits. Such a feature may be challenging for spacecraft operations, and orbital maneuvers should be carefully planned.

The mission and aerocapture vehicle design presented in Girija (2023) to achieve a $4\,000 \times 550\,000 \text{ km}$ trajectory is adapted here to achieve a smaller $2\,000 \times 100\,000 \text{ km}$ elliptical, polar orbit. Its apocentre is just outside the Uranian ring system. Such a relatively small orbit is beyond the reach of conventional propulsive insertion due to the large ΔV required, but it turns out to be feasible using aerocapture. Using a vehicle with lift-to-drag (L/D) = 0.24, the Theoretical Corridor Width (TCW) for aerocapture is 1.22° , which is sufficient to accommodate delivery errors and atmospheric uncertainties. Figure 6 shows the overshoot and undershoot limit trajectories for an aerocapture vehicle targeting a $100\,000 \text{ km}$ apocentre altitude at atmospheric exit using the Aerocapture Mission Analysis Tool by Girija et al. (2021).

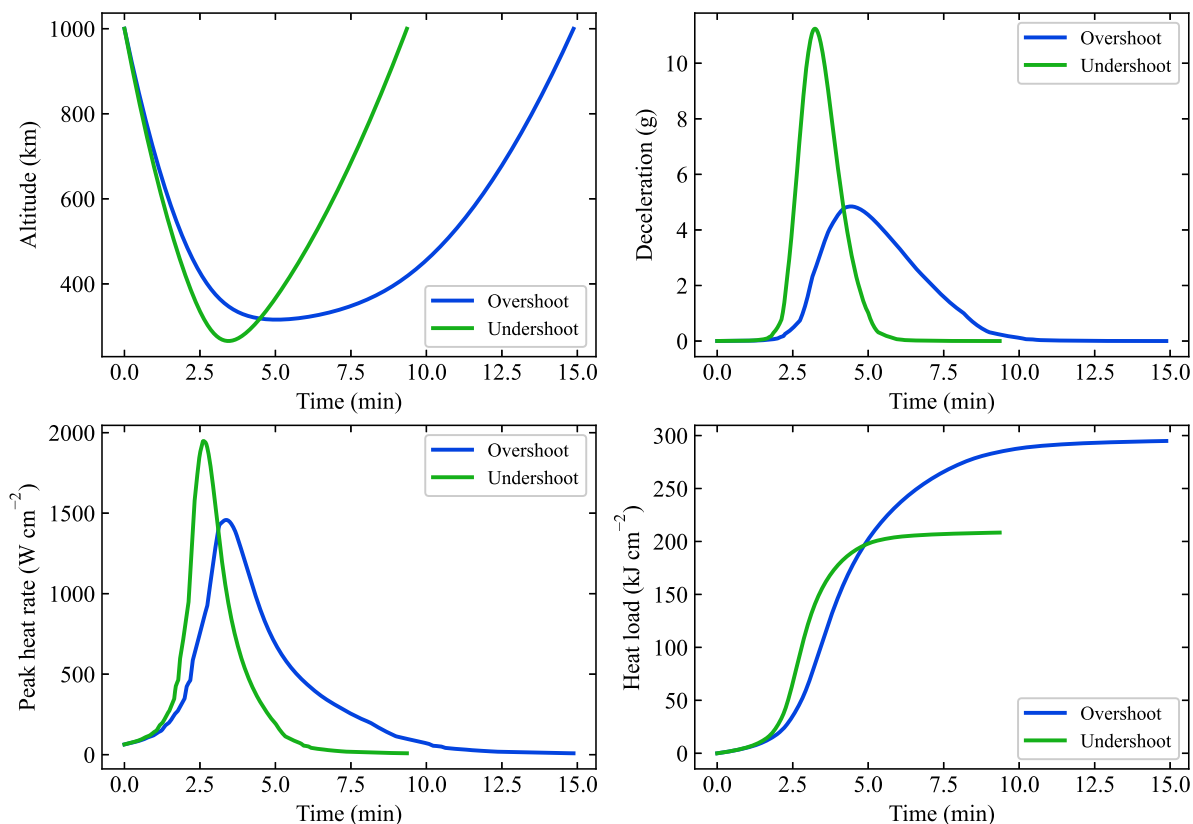


Fig. 6.— Overshoot and undershoot trajectories for a Mars Science Laboratory (MSL)-derived aerocapture vehicle with lift-to-drag $L/D = 0.24$, ballistic coefficient $\beta = 146 \text{ kg m}^{-2}$, spacecraft nose radius $R_n = 1.125 \text{ m}$, $h_{\text{apo}} = 100\,000 \text{ km}$. The independent variable on the horizontal axes is the time since entry interface, defined at 1000 km above the 1 bar pressure level, while the unit of measure for the deceleration denoted as “g” in the vertical axis of the panel in the upper right corner is the mean Earth’s acceleration of gravity.

The peak heat rate is estimated to be in the range of 1 500 to 2 000 W cm⁻², which is well within the capability of the Heatshield for Extreme Entry Environment Technology (HEEET) (Venkatapathy et al. 2020). At the first apocentre, the spacecraft performs a 120 m s⁻¹ propulsive burn to raise the pericentre outside the atmosphere and achieve its 2 000 × 100 000 km elliptical capture orbit.

Using a different aerocapture vehicle design known as drag modulation, it is possible to send a small orbiter with, say, a mass of 200 kg, into a 2 000 × 10 000 km as a secondary spacecraft carried by the main orbiter. The orbit is so small that the ΔV for its insertion exceeds 12 km s⁻¹. However, with aerocapture such an orbital configuration is achievable. It would also be considered too risky for a large orbiter, and presents engineering challenges such as the spacecraft frequently going behind Uranus as viewed from Earth and orbit decay due to drag from the upper atmosphere. A small spacecraft can accommodate the risks while providing measurements from the low-circular orbit which cannot be made otherwise. The small orbiter will detach from the mothership a few weeks prior to entry, and use aerocapture to insert into a near-circular orbit around Uranus. The apocentre is just inside the rings, which start at $\approx 12\,500$ km. Using a drag modulation vehicle with⁸ $\beta_1 = 10 \text{ kg m}^{-2}$ and $\beta_2/\beta_1 = 7.5$ offers a TCW of 0.70° for aerocapture to a $h_{\text{apo}} = 10\,000$ km. Figure 7 shows the nominal aerocapture trajectory of the latter. At the first pericentre, the spacecraft performs a 200 m s⁻¹ propulsive burn to achieve its initial capture orbit of 2 000 × 10 000 km.

⁸The parameters β_1 and β_2 are the values of the ballistic coefficient β before and after the drag skirt separation, respectively, for drag modulation aerocapture. The ballistic coefficient ratio β_2/β_1 is a key design parameter indicating how much control authority the vehicle has.

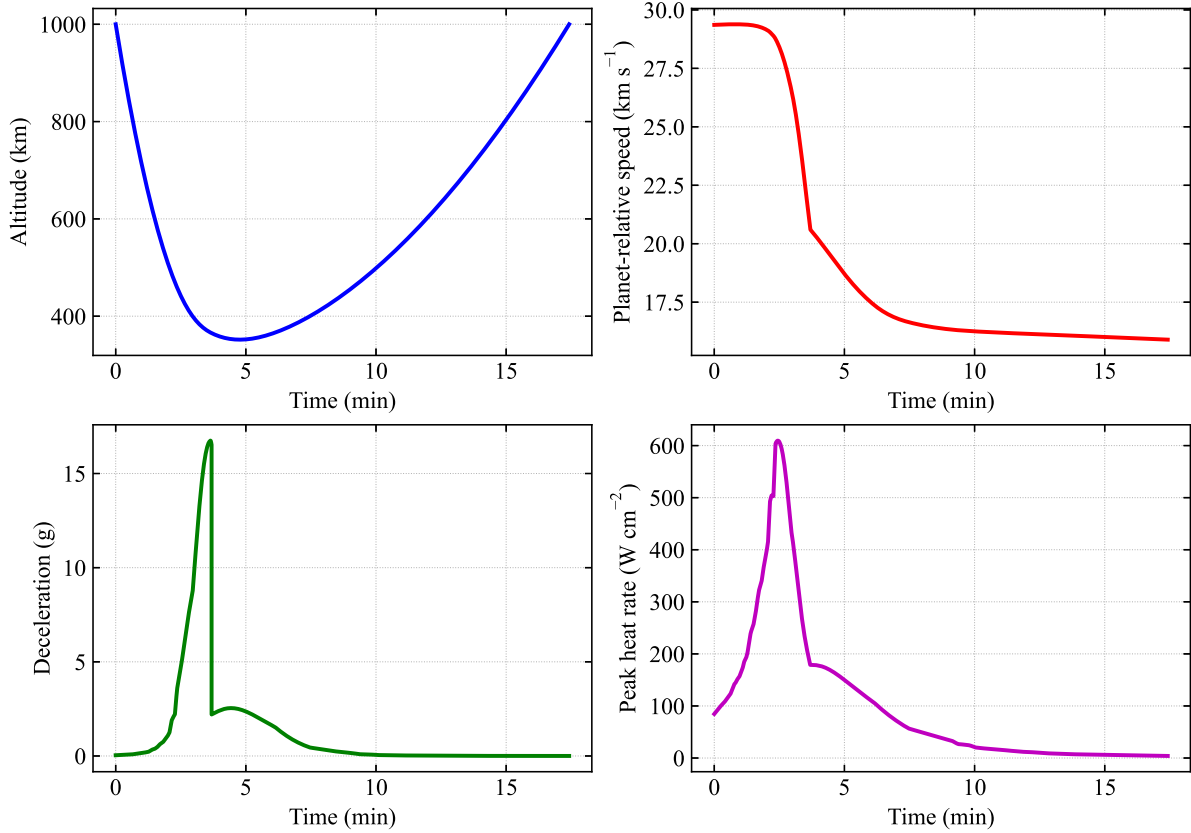


Fig. 7.— Nominal drag modulation trajectory for a vehicle with ballistic coefficient before the drag skirt separation $\beta_1 = 10 \text{ kg m}^{-2}$, ballistic coefficient ratio $\beta_2/\beta_1 = 7.5$, and apocentre altitude $h_{\text{apo}} = 10\,000 \text{ km}$. The independent variable on the horizontal axes is the time since entry interface, defined at 1 000 km above the 1 bar pressure level, while the unit of measure for the deceleration denoted as “g” in the vertical axis of the panel in the lower left corner is the mean Earth’s acceleration of gravity.

7. Summary and conclusions

A mission concept, provisionally dubbed EURO (Elliptical Uranian Relativity Orbiter), based on the use of a spacecraft around Uranus to measure the planet’s angular momentum $S_{\hat{k}_{\Upsilon}}$ by means of its general relativistic LT orbital precessions independently of the Newtonian ones induced by the planetary gravity field’s zonal multipoles J_{ℓ} , $\ell = 2, 3, 4, \dots$ was presented.

The orbital geometry allowing, in principle, the fulfillment of such a goal implies an orbital plane perpendicular to the CE and containing the Uranian spin axis \hat{k}_{Υ} . Moreover, its node Ω is equal to the right ascension $\alpha_{\hat{k}_{\Upsilon}}$ of \hat{k}_{Υ} . Indeed, in this case, the classical precessions of the orbital inclination I and of Ω due to the even and odd zonals of the planet’s gravity field ideally vanish, contrary to the gravitomagnetic ones. The situation is reversed for the precessions of the argument of pericentre ω .

For a $2\,000 \times 100\,000$ km orbit, it turns out that the general relativistic rates of I and Ω amount to $\simeq 16 - 59$ mas yr $^{-1}$, while the size of the Newtonian pericentre precession due to J_2 is as large as $\simeq 173^{\circ}$ yr $^{-1}$. An approximate evaluation of the LT net shift per orbit of the range-rate yields $\simeq 2 \times 10^{-4}$ mm s $^{-1}$ for a suitable choice of the initial conditions, with a peak-to-peak amplitude up to $\simeq 1.5 \times 10^{-3}$ mm s $^{-1}$ for a single passage at the pericentre few hours long. Such figures are demanding with respect to the $\simeq 10^{-2}$ mm s $^{-1}$ accuracy level of, say, Juno, posing a challenge to the success of the mission. By lowering the apocentre height down to 10 000 km, it is possible to increase the relativistic signatures to the level of $\simeq 100 - 400$ mas yr $^{-1}$.

A major source of systematic bias is represented by the accuracies with which the orientation of \hat{k}_{Υ} and I should be determined. It turns out that they are of the order of $\simeq 0.1 - 1$ mas and $\simeq 1 - 10$ mas, respectively; the pole of Uranus is currently known with an accuracy of $\simeq 7$ arcsec due to the lack of dedicated, in-situ mission(s). To this aim, it is conceivable that a possible “phase 1” of the EURO mission may allow for good enough measurements of \hat{k}_{Υ} and I by standard geodetic techniques.

Using the LT effect to dynamically measure the spin angular momentum of Uranus is definitely a challenging task.

Acknowledgements

One of us (L.I.) is grateful to L. Iess and L. Petrov for useful information. All the authors thank the referee for her/his attentive and constructive remarks.

Data availability

Aerocapture trajectory results presented in the study can be reproduced using Jupiter Notebooks available at <https://amat.readthedocs.io/en/master/other-notebooks.html#euro-uranus-orbiter>. The study results were made with AMAT v2.2.22. An archived version of AMAT v2.2.22 is available at Zenodo. DOI:10.5281/zenodo.7542714

REFERENCES

- Arridge C. S. et al., 2014, *Planet. Space Sci.*, 104, 122
- Arridge C. S. et al., 2012, *Exp. Astron.*, 33, 753
- Barker B. M., O’Connell R. F., 1975, *Phys. Rev. D*, 12, 329
- Bergstrahl J. T., Miner E. D., Matthews M. N., eds., 1991, *Uranus*. The University of Arizona Press, Tucson
- Bertotti B., Farinella P., Vokrouhlický D., 2003, *Physics of the Solar System*. Kluwer, Dordrecht
- Bertotti B., Iess L., Tortora P., 2003, *Nature*, 425, 374
- Bocanegra-Bahamón T. et al., 2015, *Adv. Space Res.*, 55, 2190
- Bolton S., ed., 2018, *The Juno Mission*. Springer, Dordrecht
- Braginsky V. B., Caves C. M., Thorne K. S., 1977, *Phys. Rev. D*, 15, 2047
- Brouwer D., Clemence G. M., 1961, *Methods of Celestial Mechanics*. Academic Press, New York
- Brumberg V. A., 1991, *Essential Relativistic Celestial Mechanics*. Adam Hilger, Bristol
- Burgay M. et al., 2003, *Nature*, 426, 531
- Capderou M., 2005, *Satellites. Orbits and Missions*. Springer-Verlag France, Paris
- Casotto S., 1993, *Celest. Mech. Dyn. Astr.*, 55, 209
- Cattaneo C., 1958, *Nuovo Cim.*, 10, 318
- Ciufolini I. et al., 2013, *Nucl. Phys. B Proc. Suppl.*, 243, 180
- Cohen I. J. et al., 2022, *Planet. Science J.*, 3, 58
- Costa L. F. O., Herdeiro C. A. R., 2008, *Phys. Rev. D*, 78, 024021
- Costa L. F. O., Natário J., 2014, *Gen. Relativ. Gravit.*, 46, 1792
- Costa L. F. O., Natário J., 2021, *Universe*, 7, 388
- Coulot D., Deleflie F., Bonnefond P., Exertier P., Laurain O., de Saint-Jean B., 2011, in *Encyclopedia of Solid Earth Geophysics*, Gupta H. K., ed., *Encyclopedia of Earth Sciences Series*, Springer, Dordrecht, pp. 1049–1055
- Cruikshank D. P., ed., 1995, *Neptune and Triton*. The University of Arizona Press, Tucson

- Cruz M. I., 1979, in AIAA/NASA Conference on Advanced Technology for Future Space Systems, American Institute of Aeronautics and Astronautics, Hampton, Va., pp. 195–201
- Damour T., Schäfer G., 1988, *Nuovo Cim. B*, 101, 127
- Damour T., Taylor J. H., 1992, *Phys. Rev. D*, 45, 1840
- Debono I., Smoot G. F., 2016, *Universe*, 2, 23
- Durante D. et al., 2020, *Geophys. Res. Lett.*, 47, e86572
- Dymnikova I. G., 1986, *Sov. Phys. Usp.*, 29, 215
- Everitt C. W. F. et al., 2011, *Phys. Rev. Lett.*, 106, 221101
- Fienga A., Laskar J., Exertier P., Manche H., Gastineau M., 2015, *Celest. Mech. Dyn. Astr.*, 123, 325
- Fletcher L. N. et al., 2020, *Planet. Space Sci.*, 191, 105030
- French R. G. et al., 1988, *Icarus*, 73, 349
- Galle J. G., 1846, *Mon. Not. Roy. Astron. Soc.*, 7, 153
- Genova A., Mazarico E., Goossens S., Lemoine F. G., Neumann G. A., Smith D. E., Zuber M. T., 2018, *Nat. Commun.*, 9, 289
- Gibney E., 2020, *Nature*, 579, 17
- Girija A. P., 2023, *Acta Astronaut.*, 202, 104
- Girija A. P., Saikia S., Longuski J., Cutts J., 2021, *J. Open Source Softw.*, 6, 3710
- Girija A. P., Saikia S. J., Longuski J. M., Lu Y., Cutts J. A., 2022, *J. Spacecraft Rockets*, 59, 1074
- Guillot T., 2021, *Exp. Astron.*
- Harris E. G., 1991, *Am. J. Phys.*, 59, 421
- Helled R., Fortney J. J., 2020, *Phil. Trans. R. Soc. A*, 378, 20190474
- Helled R., Nettelmann N., Guillot T., 2020, *Space Sci. Rev.*, 216, 38
- Herschel W., 1781, *Phil. Trans. Roy. Soc. London*, 71, 492
- Hofstadter M. et al., 2019, *Planet. Space Sci.*, 177, 104680
- Hu H., Kramer M., Wex N., Champion D. J., Kehl M. S., 2020, *Mon. Not. Roy. Astron. Soc.*, 497, 3118

- Hubbard W. B., 1997, in *Encyclopedia of Planetary Sciences*, Shirley J. H., Fairbridge R. W., eds., Springer, Dordrecht, pp. 856–858
- Hughes K. M., 2016, PhD thesis, Purdue University, Indiana
- Iorio L., 2017, *Eur. Phys. J. C*, 77, 439
- Iorio L., 2020, *Mon. Not. Roy. Astron. Soc.*, 495, 2777
- Iorio L., Lichtenegger H. I. M., Ruggiero M. L., Corda C., 2011, *Astrophys. Space Sci.*, 331, 351
- Iorio L., Ruggiero M. L., Corda C., 2013, *Acta Astronaut.*, 91, 141
- Jacobson R. A., 2014, *Astron J.*, 148, 76
- Jacobson R. A., 2022, *Astron J.*, 164, 199
- Jantzen R. T., Carini P., Bini D., 1992, *Ann. Phys. (N Y)*, 215, 1
- Jarmak S. et al., 2020, *Acta Astronaut.*, 170, 6
- Kehl M. S., Wex N., Kramer M., Liu K., 2017, in *The Fourteenth Marcel Grossmann Meeting. Proceedings of the MG14 Meeting on General Relativity*, Bianchi M., Jantzen R., Ruffini R., eds., World Scientific, Singapore, pp. 1860–1865
- Kopeikin S. M., Efroimsky M., Kaplan G., 2011, *Relativistic Celestial Mechanics of the Solar System*. Wiley-VCH, Weinheim
- Le Verrier U., 1846, *Cr. Hebd. Acad. Sci.*, 23, 428
- Lense J., Thirring H., 1918, *Phys. Z.*, 19, 156
- Leszczynski Z. V., 1998, Phd thesis, Naval Postgraduate School, Monterey
- Lyne A. G. et al., 2004, *Science*, 303, 1153
- Ma C. et al., 1998, *Astron J.*, 116, 516
- Mandt K. E., 2023, *Science*, 379, 640
- Mann A., 2017, *Proc. Natl. Acad. Sci.*, 114, 4566
- Mansell J. et al., 2017, *Adv. Space Res.*, 59, 2407
- Mashhoon B., 2001, in *Reference Frames and Gravitomagnetism*, Pascual-Sánchez J. F., Floría L., San Miguel A., Vicente F., eds., World Scientific, Singapore, pp. 121–132
- Mashhoon B., 2007, in *The Measurement of Gravitomagnetism: A Challenging Enterprise*, Iorio L., ed., Nova Science, New York, pp. 29–39

- Mashhoon B., Hehl F. W., Theiss D. S., 1984, *Gen. Relativ. Gravit.*, 16, 711
- Masters A., Ioannou C., Rayns N., 2022, *Geophys. Res. Lett.*, 49, e2022GL100921
- Misner C. W., Thorne K. S., Wheeler J. A., 2017, *Gravitation*. Princeton University Press, Princeton and Oxford
- Mousis O. et al., 2018, *Planet. Space Sci.*, 155, 12
- Murray C. D., Dermott S. F., 2000, *Solar System Dynamics*. Cambridge University Press, New York
- National Research Council, 2011, *Vision and voyages for planetary science in the decade 2013-2022*. Tech. rep., The National Academies Press, Washington DC
- National Research Council, 2018, *Visions into voyages for planetary sciences in the decade 2013-2022: A midterm review*. Tech. rep., The National Academies Press, Washington DC
- National Research Council, 2022, *Origins, worlds, and life. a decadal strategy for planetary science and astrobiology 2023-2032*. Tech. rep., The National Academies Press, Washington DC
- Neuenschwander B. A., Helled R., 2022, *Mon. Not. Roy. Astron. Soc.*, 512, 3124
- Park R. S., Folkner W. M., Konopliv A. S., Williams J. G., Smith D. E., Zuber M. T., 2017, *Astron J.*, 153, 121
- Pearlman M. et al., 2019, *J. Geod.*, 93, 2181
- Petit G., Luzum B., eds., 2010, *IERS Technical Note, Vol. 36, IERS Conventions (2010)*. Verlag des Bundesamts für Kartographie und Geodäsie, Frankfurt am Main
- Pitjeva E. V., Pitjev N. P., 2014, *Celest. Mech. Dyn. Astr.*, 119, 237
- Poisson E., Will C. M., 2014, *Gravity*. Cambridge University Press, Cambridge
- Pugh G. E., 1959, *Proposal for a Satellite Test of the Coriolis Prediction of General Relativity*. Research Memorandum 11, Weapons Systems Evaluation Group, The Pentagon, Washington D.C.
- Renzetti G., 2013, *Centr. Eur. J. Phys.*, 11, 531
- Rindler W., 2001, *Relativity: special, general, and cosmological*. Oxford University Press, New York
- Rogoszinski Z., Hamilton D. P., 2021, *Planet. Science J.*, 2, 78
- Ruggiero M. L., 2021, *Universe*, 7, 451

- Ruggiero M. L., Tartaglia A., 2002, *Nuovo Cim. B*, 117, 743
- Saikia S. J. et al., 2021, *J. Spacecraft Rockets*, 58, 505
- Saillenfest M., Rogoszinski Z., Lari G., Baillié K., Boué G., Crida A., Lainey V., 2022, *Astron. Astrophys.*, 668, A108
- Sayanagi K. M. et al., 2020, *Space Sci. Rev.*, 216, 72
- Schäfer G., 2004, *Gen. Relativ. Gravit.*, 36, 2223
- Schäfer G., 2009, *Space Sci. Rev.*, 148, 37
- Schiff L., 1960, *Phys. Rev. Lett.*, 4, 215
- Schubert G., Soderlund K. M., 2011, *Phys. Earth Planet. Inter.*, 187, 92
- Simon A., Nimmo F., Anderson R. C., 2021, *Journey to an Ice Giant System. Uranus Orbiter & Probe*. Technical report, National Aeronautics and Space Administration
- Soffel M. H., 1989, *Relativity in Astrometry, Celestial Mechanics and Geodesy*. Springer, Heidelberg
- Soffel M. H., Han W.-B., 2019, *Applied General Relativity, Astronomy and Astrophysics Library*. Springer Nature Switzerland, Cham
- Spilker L., 2019, *Science*, 364, 1046
- Spilker T. R. et al., 2019, *J. Spacecraft Rockets*, 56, 536
- Stella L., Possenti A., 2009, *Space Sci. Rev.*, 148, 105
- Stone E. C., 1987, *J. Geophys. Res.: Space Phys.*, 92, 14873
- Stone E. C., Miner E. D., 1986, *Science*, 233, 39
- Tacconi L. J. et al., 2021, *Voyage 2050. final recommendations from the Voyage 2050 Senior Committee*. Tech. rep., European Space Agency
- Tartaglia A., 2002, *Europhys. Lett.*, 60, 167
- Thorne K. S., 1986, in *Highlights of Modern Astrophysics: Concepts and Controversies*, Shapiro S. L., Teukolsky S. A., Salpeter E. E., eds., Wiley, New York, pp. 103–161
- Thorne K. S., 1988, in *Near Zero: New Frontiers of Physics*, Fairbank J. D., Deaver B. S. J., Everitt C. W. F., Michelson P. F., eds., Freeman, New York, pp. 573–586
- Thorne K. S., MacDonald D. A., Price R. H., eds., 1986, *Black Holes: The Membrane Paradigm*. Yale University Press, New Haven and London

Turrini D. et al., 2014, *Planet. Space Sci.*, 104, 93

Venkatapathy E. et al., 2020, *Space Sci. Rev.*, 216, 22

Venkatraman Krishnan V. et al., 2020, *Science*, 367, 577

Will C. M., 2018, *Theory and Experiment in Gravitational Physics*. Second edition. Cambridge University Press, Cambridge

Will C. M., Nordtvedt K. J., 1972, *ApJ*, 177, 757

Witze A., 2022, *Nature*, 604, 607

Xu L., Zou Y., Jia Y., 2018, *Chin. J. Space Sci.*, 38, 591–592

Appendix A The averaged rates of I , Ω , ω due to some even and odd zonal harmonics

The averaged rates of the inclination I , of the longitude of the ascending node Ω , and of the argument of pericentre ω induced by the zonal harmonics J_ℓ of degree $\ell = 2, 3, 4, \dots$ of the multipolar expansion of the classical part of the gravitational potential of a non-spherical body can be computed, e.g., with the planetary equations in the form of Lagrange (Bertotti, Farinella & Vokrouhlický 2003)

$$\dot{I}^{J_\ell} = \frac{1}{n_b a^2 \sqrt{1-e^2} \sin I} \left(\frac{\partial \langle \Delta U_\ell \rangle}{\partial \Omega} - \cos I \frac{\partial \langle \Delta U_\ell \rangle}{\partial \omega} \right), \quad (\text{A.1})$$

$$\dot{\Omega}^{J_\ell} = -\frac{1}{n_b a^2 \sqrt{1-e^2} \sin I} \frac{\partial \langle \Delta U_\ell \rangle}{\partial I}, \quad (\text{A.2})$$

$$\dot{\omega}^{J_\ell} = \frac{\cot I}{n_b a^2 \sqrt{1-e^2}} \frac{\partial \langle \Delta U_\ell \rangle}{\partial I} - \frac{\sqrt{1-e^2}}{n_b a^2 e} \frac{\partial \langle \Delta U_\ell \rangle}{\partial e}, \quad (\text{A.3})$$

where

$$\langle U_\ell \rangle = \frac{n_b}{2\pi} \int_{f_0}^{f_0+2\pi} \Delta U_\ell \frac{dt}{df} df. \quad (\text{A.4})$$

In Equation (A.4), the instantaneous correction ΔU_ℓ of degree ℓ of the Newtonian monopole, to be evaluated onto an unperturbed Keplerian ellipse by means of

$$r = \frac{p}{1 + e \cos f}, \quad (\text{A.5})$$

$$\frac{dt}{df} = \frac{(1 - e^2)^{3/2}}{n_b (1 + e \cos f)^2}, \quad (\text{A.6})$$

is (Bertotti, Farinella & Vokrouhlický 2003)

$$\Delta U_\ell = \frac{\mu}{r} J_\ell \left(\frac{R}{r} \right)^\ell \mathcal{P}_\ell(\hat{\mathbf{k}} \cdot \hat{\mathbf{r}}). \quad (\text{A.7})$$

In Equation (A.7), $\mathcal{P}_\ell(\dots)$ is the Legendre polynomial of degree ℓ , and its argument, i.e. the cosine of the angle between the primary's spin axis $\hat{\mathbf{k}}$ and the position vector \mathbf{r} of the test particle, can be written as (Soffel 1989; Brumberg 1991; Soffel & Han 2019)

$$\hat{\mathbf{k}} \cdot \hat{\mathbf{r}} = (\hat{\mathbf{k}} \cdot \hat{\mathbf{l}}) \cos u + (\hat{\mathbf{k}} \cdot \hat{\mathbf{m}}) \sin u, \quad (\text{A.8})$$

where

$$u \doteq \omega + f \quad (\text{A.9})$$

is the argument of latitude.

For $\ell = 2, 3, 4, \dots, 8$, it turns out that the averaged rates of I and Ω , computed with Equations (46)–(47), vanish, contrary to the pericentre whose precessions are

$$\dot{\omega}^{J_2} = -\frac{3}{4} n_b J_2 \left(\frac{R}{p} \right)^2, \quad (\text{A.10})$$

$$e \dot{\omega}^{J_3} = -\frac{3}{8} n_b J_3 \left(\frac{R}{p} \right)^3 (1 + 4e^2) \cos \xi, \quad (\text{A.11})$$

$$\dot{\omega}^{J_4} = -\frac{15}{128} n_b J_4 \left(\frac{R}{p} \right)^4 [12 + 9e^2 + 2(2 + 5e^2) \cos 2\xi], \quad (\text{A.12})$$

$$e \dot{\omega}^{J_5} = -\frac{15}{256} n_b J_5 \left(\frac{R}{p} \right)^5 \cos \xi [8 + 75e^2 + 22e^4 + 14(e^2 + 2e^4) \cos 2\xi], \quad (\text{A.13})$$

$$\dot{\omega}^{J_6} = -\frac{105}{4,096} n_b J_6 \left(\frac{R}{p} \right)^6 [80 + 50e^2(4 + e^2) + 10(4 + 22e^2 + 7e^4) \cos 2\xi +$$

$$+3 e^2 (4 + 7 e^2) \cos 4\xi], \quad (\text{A.14})$$

$$e \dot{\omega}^{J_7} = -\frac{21}{8,192} n_b J_7 \left(\frac{R}{p}\right)^7 \cos \xi \left[200 + 3,360 e^2 + 3,570 e^4 + 592 e^6 + \right. \\ \left. +6 e^2 (180 + 685 e^2 + 136 e^4) \cos 2\xi + 33 e^4 (5 + 8 e^2) \cos 4\xi\right], \quad (\text{A.15})$$

$$\dot{\omega}^{J_8} = \frac{63}{262,144} n_b J_8 \left(\frac{R}{p}\right)^8 \left(-175 \left\{64 + 7e^2 \left[48 + 5 e^2 (8 + e^2)\right]\right\} - \right. \\ \left. -70 (96 + 944 e^2 + 970 e^4 + 135 e^6) \cos 2\xi - 154 e^2 (40 + 128 e^2 + 27 e^4) \cos 4\xi - \right. \\ \left. -286 e^4 (2 + 3 e^2) \cos 6\xi\right), \quad (\text{A.16})$$

where

$$\xi \doteq \delta - \omega. \quad (\text{A.17})$$

Note that the precessions induced by the odd zonals, i.e. Equation (A.11), Equation (A.13), and Equation (A.15), vanish if calculated with Equation (96).

Appendix B The range-rate perturbation

The velocity vector \mathbf{v} of a test particle moving along an unperturbed Keplerian ellipse around a massive primary is

$$\mathbf{v} = \{v_x, v_y, v_z\}, \quad (\text{B.1})$$

with (Kopeikin, Efroimsky & Kaplan 2011; Poisson & Will 2014)

$$v_x = -\frac{n_b a}{\sqrt{1-e^2}} [\cos \Omega (e \sin \omega + \sin u) + \cos I \sin \Omega (e \cos \omega + \cos u)], \quad (\text{B.2})$$

$$v_y = -\frac{n_b a}{\sqrt{1-e^2}} [-\cos I \cos \Omega (e \cos \omega + \cos u) + \sin \Omega (e \sin \omega + \sin u)], \quad (\text{B.3})$$

$$v_z = \frac{n_b a}{\sqrt{1-e^2}} \sin I (e \cos \omega + \cos u). \quad (\text{B.4})$$

The instantaneous change $\Delta \mathbf{v}$ of \mathbf{v} has, then, to be computed as⁹

$$\Delta \mathbf{v} = \left\{ \sum_{\kappa} \frac{\partial v_x}{\partial \kappa} \Delta \kappa(f), \sum_{\kappa} \frac{\partial v_y}{\partial \kappa} \Delta \kappa(f), \sum_{\kappa} \frac{\partial v_z}{\partial \kappa} \Delta \kappa(f) \right\}, \kappa = a, e, I, \Omega, \omega, f. \quad (\text{B.5})$$

In Equation (B.5), the instantaneous shift $\Delta \kappa(f)$ of any perturbed osculating orbital element κ among a, e, I, Ω, ω can be analytically worked out as

$$\Delta \kappa(f) = \int_{f_0}^f \frac{d\kappa}{dt} \frac{dt}{df'} df', \quad (\text{B.6})$$

where $d\kappa/dt$ is the right-hand-side of the equation for the osculating element κ in the Euler-Gauss form (Soffel 1989; Brumberg 1991; Kopeikin, Efroimsky & Kaplan 2011; Soffel & Han 2019), calculated with the disturbing acceleration \mathbf{A} at hand and evaluated onto the unperturbed Keplerian ellipse characterized by Equations (A.5)–(A.6). As per the variation Δf of the true anomaly, it is usually expressed in terms of the changes of the mean anomaly \mathcal{M} and of the eccentricity e as follows. First, the true anomaly f is written as a function of the eccentric anomaly E as (Capderou 2005)

$$\tan\left(\frac{f}{2}\right) = \sqrt{\frac{1+e}{1-e}} \tan\left(\frac{E}{2}\right). \quad (\text{B.7})$$

Then, the shift of f is calculated by differentiating Equation (B.7) with respect to e and E as

$$\Delta f = \frac{\partial f}{\partial e} \Delta e + \frac{\partial f}{\partial E} \Delta E = \frac{\sin E}{\sqrt{1-e^2} (1-e \cos E)} \Delta e + \sqrt{\frac{1+e}{1-e}} \frac{1-e}{(1-e \cos E)} \Delta E \quad (\text{B.8})$$

In turn, from the Kepler equation (Capderou 2005)

$$\mathcal{M} = E - e \sin E, \quad (\text{B.9})$$

one gets

$$\Delta E = \frac{\Delta \mathcal{M} + \sin E \Delta e}{1 - e \cos E}. \quad (\text{B.10})$$

Finally, by inserting Equation (B.10) in Equation (B.8) and using (Capderou 2005)

$$r = a (1 - e \cos E), \quad (\text{B.11})$$

$$\sin E = \frac{\sqrt{1-e^2} \sin f}{1 + e \cos f}, \quad (\text{B.12})$$

$$\cos E = \frac{e + \cos f}{1 + e \cos f}, \quad (\text{B.13})$$

⁹In calculating the partial derivatives with respect to a , n_b has to be considered as a function of a .

one obtains

$$\Delta f = \left(\frac{a}{r}\right) \left[\sin f \left(1 + \frac{r}{p}\right) \Delta e + \sqrt{1 - e^2} \left(\frac{a}{r}\right) \right] \Delta \mathcal{M}, \quad (\text{B.14})$$

in agreement with Casotto (1993, Eq. (A.6)).

The instantaneous perturbations $\Delta v_R(f)$, $\Delta v_T(f)$, $\Delta v_N(f)$ of the radial (R), transverse (T) and out-of-plane (N) components of the velocity are worked out by projecting Equation (B.5) onto the radial, transverse and normal directions given by the unit vectors (Soffel 1989; Brumberg 1991; Soffel & Han 2019)

$$\mathbf{u}_R = \{\cos \Omega \cos u - \cos I \sin \Omega \sin u, \sin \Omega \cos u + \cos I \cos \Omega \sin u, \sin I \sin u\}, \quad (\text{B.15})$$

$$\mathbf{u}_T = \{-\cos \Omega \sin u - \cos I \sin \Omega \cos u, -\sin \Omega \sin u + \cos I \cos \Omega \cos u, \sin I \cos u\}, \quad (\text{B.16})$$

$$\mathbf{u}_N = \{\sin I \sin \Omega, -\sin I \cos \Omega, \cos I\}. \quad (\text{B.17})$$

As a result, one gets

$$\begin{aligned} \Delta v_R(f) = \Delta \mathbf{v} \cdot \mathbf{u}_R = & -\frac{n_b \sin f}{\sqrt{1 - e^2}} \left[\frac{e \Delta a(f)}{2} + \frac{a^2 \Delta e(f)}{r} \right] - \\ & - \frac{n_b a^2 \sqrt{1 - e^2}}{r} [\cos I \Delta \Omega(f) + \Delta \omega(f)] - \frac{n_b a^3}{r^2} \Delta \mathcal{M}(f), \end{aligned} \quad (\text{B.18})$$

$$\begin{aligned} \Delta v_T(f) = \Delta \mathbf{v} \cdot \mathbf{u}_T = & -\frac{n_b a \sqrt{1 - e^2}}{2r} \Delta a(f) + \frac{n_b a (e + \cos f)}{(1 - e^2)^{3/2}} \Delta e(f) + \\ & + \frac{n_b a e \sin f}{\sqrt{1 - e^2}} [\cos I \Delta \Omega(f) + \Delta \omega(f)], \end{aligned} \quad (\text{B.19})$$

$$\Delta v_N(f) = \Delta \mathbf{v} \cdot \mathbf{u}_N = \frac{n_b a}{\sqrt{1 - e^2}} [(\cos u + e \cos \omega) \Delta I(f) + \sin I (\sin u + e \sin \omega) \Delta \Omega(f)], \quad (\text{B.20})$$

which agree just with Casotto (1993, Eqs. (33)-(35)). Thus, the perturbation of the velocity vector can be expressed as

$$\Delta \mathbf{v} = \Delta v_R \mathbf{u}_R + \Delta v_T \mathbf{u}_T + \Delta v_N \mathbf{u}_N, \quad (\text{B.21})$$

where Δv_R , Δv_T , Δv_N are given by Equations (B.18)–(B.20), and the unit vectors \mathbf{u}_R , \mathbf{u}_T , \mathbf{u}_N are as per Equations (B.15)–(B.17).

In case of a spacecraft orbiting a distant planet P, the dynamical¹⁰ component of the range-rate $\dot{\rho}$ is the projection of the planetocentric velocity \mathbf{v} onto the unit vector $\hat{\rho}$ of the line of sight which can be approximated with the opposite of the versor of the geocentric position vector $\hat{\mathbf{R}}$ of P. Usually, the latter remains constant during a fast passage of the probe at the pericentre, or even during a full orbital revolution. In terms of the RA ϕ and DEC χ of P, it can be written as

$$\hat{\rho} \simeq -\hat{\mathbf{R}} = -\{\cos \chi \cos \phi, \cos \chi \sin \phi, \sin \chi\}. \quad (\text{B.22})$$

Thus, the range-rate perturbation $\Delta\dot{\rho}$ can be analytically calculated by means of Equation (B.21) and Equation (B.22) as

$$\Delta\dot{\rho} = \Delta\mathbf{v} \cdot \hat{\rho} \simeq -\Delta\mathbf{v} \cdot \hat{\mathbf{R}}. \quad (\text{B.23})$$

Appendix C Naming the apsidal positions in the case of Uranus

Here, some proposals for properly naming the pericentre and apocentre in the case of Uranus are given.

The first suggestion is “periouranon” and “apouranon”, from περί+ Οὐρανός (perí+Ūranós) and ἀπό+ Οὐρανός (apó+Ūranós), respectively. Indeed, Οὐρανός is the Greek god personifying the sky after whom the seventh planet of the solar system was named, while περί (+ accusative) and ἀπό (+ genitive) are prepositions meaning *around*, *near*, *about*, and *from*, *away from*, respectively. One might be tempted to propose the term “aphouranon”, as in “aphelion” for the Sun. Actually, the former should be avoided since the apocopic form ἀφ’ (aph’) of ἀπό is used before a vowel with rough breathing (´), as just in Ἥλιος (Hélios), while Οὐρανός has the smooth breathing (˘).

As an alternative proposal, “pericælum” and “apocælum” could also be considered since *Cælūs* is the Roman counterpart of Οὐρανός.

Should one rely upon the colour of the planet, “pericærum” and “apocærum” could be adopted, from the Latin adjective *cæruleus* meaning, among other things, just “greenish-blue”.

¹⁰It means that it is solely due to the planetocentric orbital motion of the probe; it neglects all the special and general relativistic effects connected with the propagation of the electromagnetic waves through a variable gravitational field (Kopeikin, Efroimsky & Kaplan 2011).